Communication in Physical Sciences, 2025, 12(8):2323-2340

Kinetic Studies on the Sequestration of Pb^{2+} and Ni^{2+} Ions in Aqueous Solutions Using Manganese Nanoparticles Anchored in Ixora Coccinea

Felicia Uchechukwu Okwunodulu*, Okechukwu Chimereoke Lord Ubani, Immaculate Nnedimma Onaka and Emeka Junior Chika
Received:14 October 2025/Accepted: 18 December 2025/Published: 25 December 2025
https://dx.doi.org/10.4314/cps.v12i8.12

***Abstract*:** *This study reports the green synthesis, characterization, and adsorption performance of manganese nanoparticles produced using plant extract. FTIR analysis confirmed functional group involvement through peak reductions and shifts, while XRD revealed a major diffraction peak at 28.45° with a d-spacing of 3.13 Å, indicating crystalline nanoparticle formation. The nanoparticles exhibited very high adsorption capacities for Ni^{2+} and Pb^{2+}, reaching 99.32 mg/g and 99.63 mg/g respectively within 60 minutes. Kinetic evaluation showed that pseudo-first-order and pseudo-second-order models did not adequately describe the adsorption behaviour, whereas the Elovich and intraparticle diffusion models provided better fits, indicating heterogeneous surface interactions and mixed diffusion mechanisms. The results demonstrate the potential of these nanoparticles for efficient heavy-metal removal from aqueous systems.*

***Keywords*:** *Manganese nanoparticles, functional properties, environmental applications, property performance analysis*

Felicia Uchechukwu Okwunodulu*
Department of Chemistry, Michael Okpara University of Agriculture Umudike, Nigeria.
Email: okwunodulufelicia@gmail.com
Orcid id:0000-0001-9880-0046

Okechukwu Chimereoke Lord Ubani
Department of Chemistry, Michael Okpara University of Agriculture Umudike, Nigeria.
Email: ubani.okechukwu@mouau.edu.ng

Immaculate Nnedimma Onaka
Department of Chemistry, Michael Okpara University of Agriculture Umudike, Nigeria.
Email: onakannedimma@gmail.com

Emeka Junior Chika
Department of Chemistry, Michael Okpara University of Agriculture Umudike, Nigeria.
Email: chrisjremeka@gmail.com

1.0 Introduction

Industrial, agricultural, and domestic activities continue to degrade soil and water quality globally, particularly in developing countries where uncontrolled discharge of wastewater, pesticides, fertilizers, and industrial effluents is common (McMichael *et al*., 2003; Khan *et al*., 2014). These pollutants introduce a wide range of organic and inorganic contaminants, including toxic heavy metals, into the environment (Das *et al*., 2015; Krug, 2009). Heavy metals such as Pb, Cd, Hg, As, Cr, and Ni are persistent, non-biodegradable, and pose serious health risks due to their ability to accumulate in living tissues.

Lead (Pb) is a highly toxic metal that interferes with enzymatic functions by binding to sulfhydryl groups or displacing essential metals such as calcium, iron, and zinc (Dart *et al*., 2004; Kosnett, 2006). Chronic exposure to Pb can damage the nervous system, kidneys, and other organs. Nickel (Ni) toxicity, commonly resulting from inhalation or occupational exposure, affects the respiratory tract and can induce dermatitis in sensitive individuals (Sinicropi *et al*., 2010). Because of these risks, the removal of

Pb^{2+} and Ni^{2+} from contaminated water remains a major environmental priority.

Conventional remediation techniques—such as chemical oxidation, precipitation, membrane filtration, and adsorption—are often costly, generate secondary pollutants, or show limited efficiency at low metal concentrations. Nanotechnology offers new opportunities for improved contaminant removal due to the unique physicochemical properties of nanoparticles, including large surface area, high reactivity, tunable porosity, and multiple sorption sites (Adeleye *et al*., 2016; Ahmad *et al*., 2021). Metal-based nanoparticles have therefore attracted significant interest as efficient adsorbents for wastewater treatment.

Green synthesis of nanoparticles using plant extracts has emerged as a sustainable alternative to conventional chemical methods (Garg *et al*., 2021). Phytochemicals in plant extracts act as reducing and stabilizing agents, enabling cost-effective and environmentally friendly nanoparticle production (Iravani, 2011). *Ixora coccinea*, a medicinal plant rich in flavonoids, alkaloids, and phenolic compounds, has shown great potential for the biosynthesis of metal nanoparticles.

Despite the promising properties of manganese nanoparticles for the sequestration of heavy metals, limited studies have examined the biosynthesis of manganese nanoparticles using *Ixora coccinea* and their adsorption kinetics toward Pb^{2+} and Ni^{2+} ions. Understanding the kinetic mechanisms is essential for designing efficient adsorption systems and optimizing contact time, reaction pathways, and rate-limiting steps (kelle *et* al., 2023; Ogoko *et al*., 2023)

Therefore, this study focuses on the biosynthesis of manganese nanoparticles using *Ixora coccinea* extract and evaluates their efficiency in the sequestration of Pb^{2+} and Ni^{2+} ions from aqueous solutions. Kinetic models, including pseudo-first-order, pseudo-second-order, Elovich, and intraparticle diffusion models, were applied to elucidate the adsorption mechanisms.

2.0 Materials and Methods

2.1 Collection of Plant Materials

Leaves of *Ixora coccinea* were collected in November 2022 from the College of Pure and Applied Sciences, Michael Okpara University of Agriculture, Umudike, Umuahia, Abia State, Nigeria. The samples were taken to the Taxonomy Section of the Forestry Department for proper identification and authentication**.**

2.2 Preparation of Aqueous Plant Extract

The extract preparation followed Constance *et al*. (2020) with minor modifications. Fresh leaves were washed thoroughly with running tap water to remove debris, rinsed with distilled water, and air-dried at room temperature. The leaves were chopped into small pieces, and 10 g of the material was boiled in 100 cm^3 of distilled water at 60 °C for 20 minutes until the solution changed from colourless to light brown. The mixture was cooled and filtered through Whatman No. 1 filter paper to obtain the aqueous extract.

2.3 Synthesis of Manganese (Mn) Nanoparticles

In the synthesis of the nanoparticle, 300 mL of the leaf extract was added to 700 mL of 9×10^{-3} M MnO_2 solution in a 1 L reaction bottle and stirred for 30 minutes. Within 24 hours, the mixture exhibited a colour change from light orange to dark orange, indicating nanoparticle formation. The nanoparticles were purified by centrifugation at 4000 rpm for 15 minutes, dried in an oven at 80 °C, allowed to cool, and stored in an airtight container. The method followed Hasan *et al*. (2023) with slight modifications.

2.4 FT-IR Spectroscopy Measurement

FT-IR analysis of the *Ixora coccinea* extract and the synthesized Mn nanoparticles was

conducted using an Agilent Cary 630 FT-IR spectrophotometer. Spectra were obtained in transmittance mode using the KBr pellet method, at a resolution of 8 cm^{-1} over the range of 4000–650 cm^{-1}.

2.5 Scanning Electron Microscopy (SEM) Analysis

The surface morphology of the nanoparticles was examined using a Phenom ProX Scanning Electron Microscope (Phenom World, Eindhoven, Netherlands), operated at magnifications of 80x to 150x. Images were used to determine shape, particle distribution, and surface characteristics.

2.6 X-ray Diffraction (XRD) Analysis

XRD patterns were recorded using a PANalytical Empyrean diffractometer (Netherlands), operated at 45 kV and 40 mA with Cu Kα radiation (λ = 0.1541 nm) in a 2θ configuration. The dried sample was finely ground, mounted on a clean glass slide, inserted into the sample holder, and analysed after instrument calibration and parameter adjustment.

2.7 Preparation of Metal Ion (Adsorbate) Solutions

Analytical-grade $NiSO_4 \cdot 6H_2O$ and $Pb(NO_3)_2$ were used to prepare 1000 mg/L stock solutions of Ni^{2+} and Pb^{2+} in deionized water, following Uchechukwu *et al*. (2015). One gram of each salt was dissolved in 1000 cm^3 of deionized water in a volumetric flask to obtain the stock solutions. From these, 5 cm^3 aliquots were diluted to 50 mL with deionized water to obtain 100 mg/L working solutions used for adsorption studies.

2.8 Effect of Contact Time on Adsorption of Ni^{2+} and Pb^{2+} Ions

Contact time studies followed Hassan *et al*. (2022) with appropriate modifications. For each metal ion, 60 cm^3 of the 100 mg/L solution was placed in separate flasks containing 1 g of Mn nanoparticles (average size 21.3 nm). The mixtures were agitated at 25 °C and pH 7.5 for 30, 60, 90, 120, and 150 minutes. After each time interval, the suspensions were filtered and the filtrates collected in labelled bottles.

Residual metal concentrations were determined using an Atomic Absorption Spectrophotometer (Buck Model 200A). The amount of metal adsorbed (Q_e, mg/g) was calculated using the mass-balance equation (Bhatti *et al*., 2007)

$$Q_e = C_0 - C_e \quad (1)$$

where Q_e defines the amount of metal adsorbed at equilibrium (mg/g), C_0 is the initial metal ion concentration (mg/L) and C_e is the final (equilibrium) concentration in solution (mg/L)

3.0 Results and Discussion

3.1 Fourier transform infrared spectroscopy

FTIR spectroscopy was conducted on the *Ixora coccinea* leaf extract before and after the biosynthesis of manganese nanoparticles (MnNPs) to identify the functional groups responsible for metal ion reduction, stabilization, and capping. The spectra and peak assignments are presented in Tables 1 and 2, while Figs. 1 and 2 display the corresponding FTIR profiles.

3.1.1 FTIR Analysis of Ixora coccinea Leaf Extract

The FTIR spectrum of the *Ixora coccinea* leaf extract (Fig. 1), supported by the peak assignments summarized in Table 1, confirms the presence of a wide range of phytochemicals capable of reducing and stabilizing manganese ions. The broad and intense absorption envelope between 3425–3850 cm^{-1} (Table 1) corresponds to O–H stretching vibrations of alcohols and phenolic compounds. This strong band reflects the abundance of hydroxyl-rich biomolecules such as flavonoids, polyphenols, tannins, and saponins, which are known electron donors during nanoparticle synthesis.

The characteristic bands at 2926.0 cm^{-1} and 2856.1 cm^{-1} indicate aliphatic C–H stretching vibrations typical of alkanes and long-chain hydrocarbons, suggesting the presence of lipids, terpenoids, and other hydrocarbon-based metabolites. A distinct peak at 2124.6 cm^{-1} (Table 1) indicates C≡C stretching of terminal alkynes, pointing to the presence of polyacetylene-type compounds. In the fingerprint region, several peaks provide further insight into the molecular complexity of the extract.

The strong absorption at 1744.4 cm^{-1} is attributed to C=O stretching of esters, while the cluster of bands between 1513–1461 cm^{-1} reflects aromatic C=C and C–C bending, confirming the presence of aromatic phytochemicals.

Table 1: FTIR Peaks of *Ixora coccinea* Leaf Extract

Peak (cm^{-1})	Assigned Functional Group	Interpretation / Possible Biomolecules
3850–3425	O–H stretching (alcohols, phenols)	Flavonoids, polyphenols, tannins
2926.0	C–H stretching (alkane)	Lipids, terpenoids
2856.1	C–H vibration (alkane)	Hydrocarbon chains
2124.6	C≡C stretching (alkyne)	Polyacetylenes
1744.4	C=O stretching (ester)	Fatty acid esters
1513–1461	Aromatic C=C / C–C bending	Aromatic phytochemicals
1244.9	C–O stretching (esters)	Esterified biomolecules
1162.9–723.3	C–O, C–H bending, aromatic out-of-plane	Carbohydrates, aromatics

Table 2: FTIR Peaks of Mn Nanoparticles

Peak (cm^{-1})	Functional Group	Interpretation / Role in Nanoparticle Formation
3251.6	O–H stretching (weakened)	Residual hydroxyls; O–H partly consumed
2094–2001	Possible weak C=O overtone	Structural modification after reduction
1613.9	C=C stretching (conjugated)	Reduction product of alkyne → alkene
1423.8	C–C bending (alkane)	Residual biomolecule structure
1334.4	C–O stretching (alcohol/phenol)	Mn–O–biomolecule capping
1263.6	C–O stretching (ester)	Stabilizing ester groups
1066.0	C–O stretching (alcohol/carbohydrate)	Strong evidence of capping by polysaccharides
831.2–745.5	Aromatic C–H bending	Indicates phytochemical binding
~650–750 (broad)	Mn–O stretching	Confirmatory evidence of MnNP formation

Additional signals at 1244.9 cm^{-1} and within 1162.9–723.3 cm^{-1} correspond to various C–O and C–H bending modes associated with Finallyesters, carbohydrates, and aromatic compounds. These combined spectral features indicate that the extract contains multiple functional groups capable of participating in metal ion reduction and surface capping. Finally, the FTIR profile of the extract (Fig. 1; Table 1) establishes a phytochemical environment rich in hydroxyl, carbonyl, aromatic, and carbohydrate groups, which are expected to drive Mn ion reduction while simultaneously stabilizing the surface of the synthesized nanoparticles.

3.1.2 FTIR Analysis of Mn Nanoparticles

The FTIR spectrum of the synthesized manganese nanoparticles (MnNPs) (Fig. 2), in agreement with the functional group assignments listed in Table 2, reveals significant spectral modifications compared to the leaf extract, confirming that the plant biomolecules actively participated in reduction and nanoparticle stabilization.

A key change is the emergence of a strong peak at 1613.9 cm^{-1}, assigned to C=C stretching of conjugated alkenes (Table 2). This shift, accompanied by the disappearance of the original alkyne signal at 2124.6 cm^{-1} (Table 1), supports the transformation of C≡C groups into conjugated C=C systems during the reduction process. This suggests that some phytochemicals underwent structural rearrangements while donating electrons to Mn ions.

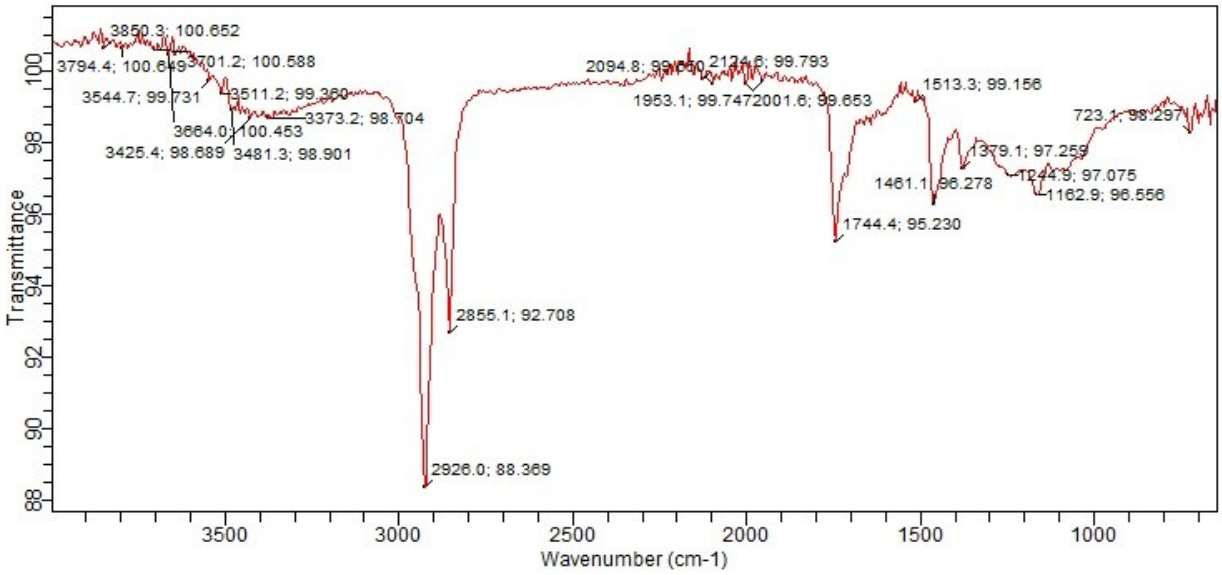

Fig. 1: FTIR Spectrum of Ixora coccinea extract

The persistence of C–O related peaks at 1334.4 cm^{-1}, 1263.6 cm^{-1}, and 1066.0 cm^{-1} (Table 2) indicates that alcohol, phenolic, ester, and carbohydrate-based groups became attached to or coordinated with the nanoparticle surface, acting as capping and stabilizing agents. These shifts relative to the extract spectrum demonstrate interaction between bio-organic molecules and the forming MnNPs, involving processes such as ligand coordination, hydrogen bonding, and surface adsorption.

A weakened O–H stretching band at 3251.6 cm^{-1} (Table 2), much narrower than the broad O–H band in the extract (Fig. 1), shows that many hydroxyl groups were consumed during the redox process. Meanwhile, the newly developed low-frequency band within ~650–

750 cm^{-1}, assigned to Mn–O stretching, provides direct evidence of manganese oxide nanoparticle formation. Additional weaker absorption bands between 745–1200 cm^{-1} further support the presence of metal–oxide–phytochemical complexes (Table 2).

Together, the spectral features of Fig. 2 and Table 2 confirm successful synthesis of MnNPs and show that oxygenated biomolecules—particularly polyphenols, carbohydrates, esters, and aromatic compounds—played an essential role not only in reducing Mn ions but also in capping the nanoparticle surface.

A comparative FTIR analysis (Figs. 1 and 2; Tables 1 and 2) of both spectra indicates a clear progression from biomolecule-rich plant extract to surface-stabilized Mn nanoparticles. The disappearance of the alkyne band, the weakening of O–H intensity, the appearance of conjugated C=C peaks, and the emergence of Mn–O vibrations all signify the chemical transformation induced by nanoparticle synthesis. Simultaneously, shifts in C–O and C=O stretching frequencies confirm that plant-derived polyphenols, esters, alcohols, and carbohydrates remain associated with the MnNP surface, providing steric and electrostatic stabilization.

The results presented in Table 3 show that several prominent peaks in the leaf extract spectrum either disappeared or decreased in intensity in the MnNP spectrum. The strong and broad O–H stretching band observed in the extract was significantly diminished in the nanoparticle spectrum, indicating that hydroxyl groups played a major role in reducing Mn ions to form nanoparticles. This reduction in O–H intensity also suggests extensive deprotonation, which is characteristic of plant-mediated redox reactions. Similarly, the disappearance or weakening of the C–H stretching bands at 2926 and 2856 cm^{-1} implies that alkane groups either engaged in capping the nanoparticle surface or underwent structural rearrangements during synthesis. The complete loss of the C≡C alkyne peak at 2124 cm^{-1} in the MnNP spectrum provides evidence that alkyne-containing phytochemicals participated actively in redox activity, converting C≡C bonds into conjugated C=C systems as reflected by the appearance of new peaks in the nanoparticle spectrum.

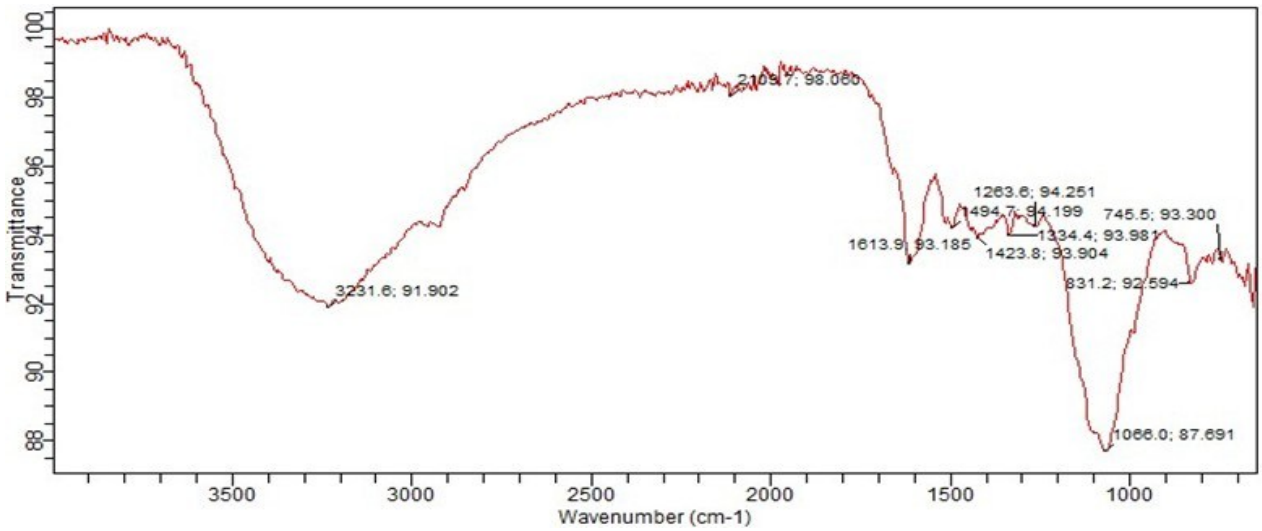

Fig. 2: FT-IR Spectrum of Manganese Nanoparticles

Table 3: Comparative FTIR Features of Leaf Extract and Mn Nanoparticles

Functional Group	Leaf Extract	MnNPs	Interpretation
O–H stretch (3400–3800 cm^{-1})	Strong	Significantly reduced	Indicates deprotonation and active involvement in Mn ion reduction
C–H alkane (2926 & 2856 cm^{-1})	Present	Weak or absent	Suggests participation of C–H groups in capping or structural modification
C≡C alkyne (2124 cm^{-1})	Present	Absent	Demonstrates reduction of alkyne to alkene during phytochemical redox activity

Further examination of the spectra reveals the presence of shifted or newly formed bands, particularly the appearance of a distinct C=C stretching peak at approximately 1613.9 cm^{-1} in the nanoparticle spectrum. This peak indicates chemical modification of the phytochemicals during nanoparticle formation, supporting the conclusion that the reducing agents in the extract underwent structural transformation. Enhanced C–O stretching signals between 1066 and 1334 cm^{-1} in the MnNP spectrum suggest the formation of metal–oxygen–biomolecule complexes, which play a crucial role in nanoparticle stabilization. These changes coincide with an overall increase in intensity across the fingerprint region, indicating successful capping of the nanoparticle surface by bio-organic molecules.

The involvement of specific functional groups in nanoparticle synthesis becomes evident from these transformations. Hydroxyl groups from alcohols and phenols served as the primary reducing agents, promoting the conversion of Mn^{2+} ions into Mn nanoparticles through electron donation and deprotonation. Alkyne and alkane groups contributed additional reducing electrons or underwent rearrangement during the reaction. Carbonyl and C–O groups provided active binding sites that attached to the nanoparticle surface, thereby preventing aggregation and ensuring stability of the synthesized MnNPs.

Although the Mn–O band is not explicitly labelled in the spectra, the presence of intensified peaks in the 1000–600 cm^{-1} region is consistent with metal–oxygen vibrations. This observation supports the formation of Mn–O bonds, further confirming successful synthesis of manganese nanoparticles. Overall, the comparative FTIR analysis clearly demonstrates that the biomolecules present in the *Ixora coccinea* extract participated directly in both the reduction of metal ions and the stabilization of the resulting nanoparticles.

3.2 Scanning electron microscopy analysis (SEM)

The surface morphology and structural features of the synthesized manganese nanoparticles were examined using SEM at magnifications of 500× (Fig. 3), 600× (Fig. 4), and 800× (Fig. 5). The three micrographs provide complementary information on particle shape, texture, aggregation tendencies, and possible influence of plant-derived biomolecules on nanoparticle formation.

Fig. 3, captured at 500× magnification, presents an overview of the nanoparticle assembly, revealing a heterogeneous distribution of elongated, fibrous, and rod-like structures dispersed across the field of view. The particles exhibit varying lengths and

diameters, suggesting that the biosynthesis process produced a mixture of morphologies rather than uniform spherical nanoparticles. The fibrous and crystalline appearance is consistent with the presence of bio-organic residues, likely originating from cellulose or lignocellulosic components within the *Ixora coccinea* extract. A few clusters can be seen, indicating early stages of agglomeration, which is expected in biologically synthesized metal nanoparticles due to the interaction between metal nuclei and organic stabilizers.

Fig. 4, recorded at 600× magnification, provides a clearer visualization of the rod-like structures observed earlier. At this magnification, the nanoparticles appear slightly more defined, with sharper edges and more distinguishable boundaries between individual particles. The increase in detail highlights the irregularity of sizes and shapes, confirming that the biosynthetic route promotes anisotropic growth. The persistence of fibrous textures further supports the involvement of plant-derived compounds, possibly polysaccharides or phenolic structures, which may have acted as templates during nanoparticle formation. Moderate aggregation is visible, likely due to inter-particle attraction or insufficient steric stabilization by the phytochemicals.

Fig. 5, taken at 800× magnification, reveals a more refined view of the nanoparticle surfaces. The rod-like and fibrous features become more prominent, and the crystalline texture is more clearly defined. At this magnification, individual particles can be differentiated from agglomerates, showing non-uniform lengths and widths characteristic of biomolecule-mediated anisotropic crystallization. The rough surface texture observed on many of the rods suggests the presence of phytochemical capping layers, an indication that the biomolecules not only reduced the manganese ions but also coated the nanoparticles during stabilization. The absence of visible porosity across the micrographs confirms that the nanoparticles formed dense, compact structures typical of plant-mediated metal nanoparticles.

When compared collectively, the three SEM images demonstrate consistent morphological characteristics—fibrous, rod-like, and irregularly shaped nanoparticles with evidence of limited clustering. Increasing magnification reveals progressively more detailed surface features, confirming that the structural characteristics are not artefacts but intrinsic to the biosynthesis process. The stability of the morphological patterns across magnifications reinforces the conclusion that plant extract constituents influenced nanoparticle nucleation and growth.

The SEM results correlate strongly with the FTIR findings. The weakened O–H band, disappearance of C≡C features, and shifts in C–O and C=O stretching vibrations indicate active participation of hydroxyl-, alkyne-, and carbonyl-containing phytochemicals in the reduction and capping processes. These functional groups, identified in the FTIR spectra, likely contributed to the fibrous and rod-like morphology observed in the SEM images by directing anisotropic growth and forming organic layers on the nanoparticle surfaces. The presence of polysaccharide-related C–O stretching bands in the FTIR spectrum aligns with the fibrous textures seen in the SEM micrographs, supporting the inference that plant-derived carbohydrates and phenolics acted as both reducing and stabilizing agents.

Overall, the SEM analysis confirms successful synthesis of manganese nanoparticles with rod-like and crystalline features, consistent with green-mediated nanoparticle formation. The morphological features observed align with the FTIR evidence of phytochemical involvement, demonstrating that biomolecules present in *Ixora coccinea* played an integral

role in shaping and stabilizing the nanoparticles.

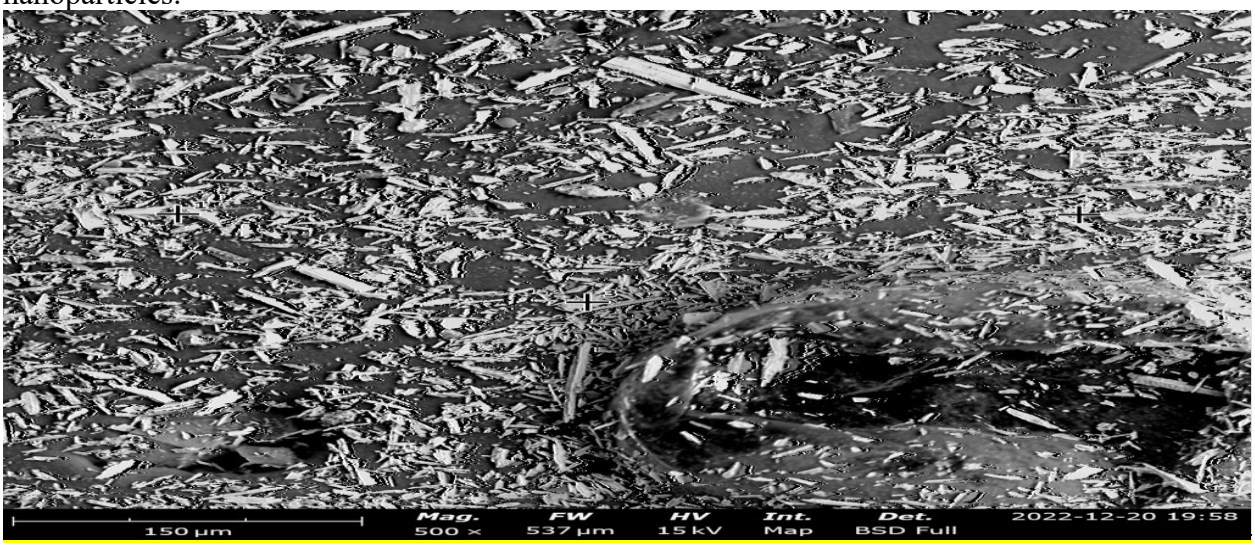

Fig. 3: SEM image (X500) of manganese nanoparticles

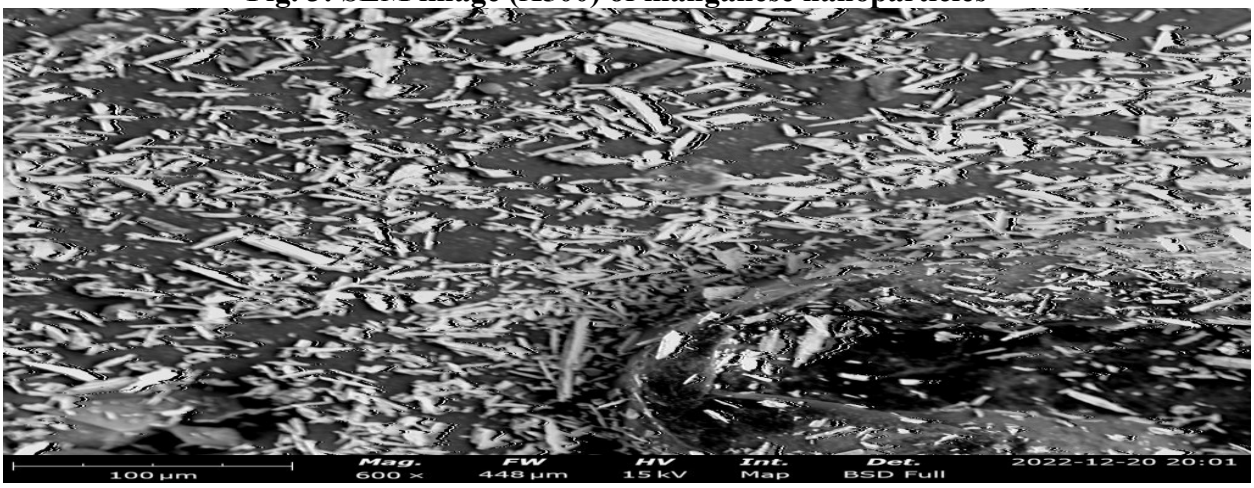

Fig 4: Zoomed SEM image (X600) of manganese nanoparticles

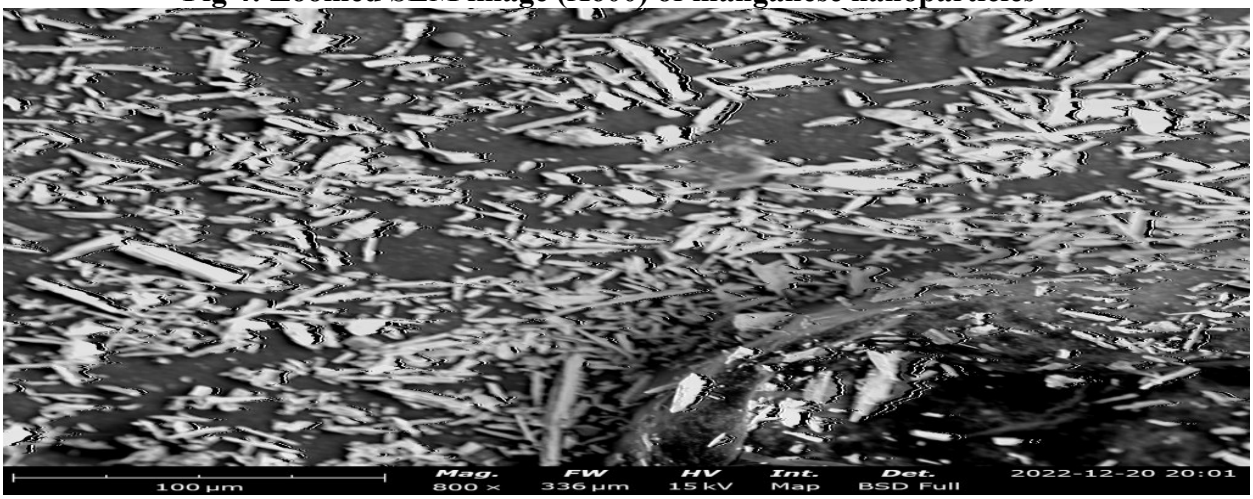

Fig. 5: Zoomed SEM (X800) image of manganese nanoparticles

3.3 X-Ray Diffraction Analysis.

3.3 X-Ray Diffraction Analysis

Fig. 6 shows the X-ray diffraction pattern of the manganese nanoparticles synthesized using the leaf extract of *Ixora coccinea*. The diffraction profile recorded from 0° to 70° revealed a broad background with a superimposed measurable crystalline reflection, indicating that the nanoparticles possessed a nanocrystalline structure with an irregular phase arrangement. A distinct Bragg peak was observed at a 2θ value of 28.4484°, which served as the primary reflection used to describe the crystalline behaviour of the synthesized material.

To further characterize this peak, the parameters extracted from the XRD pattern were compiled and presented in Table 3. Table 3 contains the positional and intensity values associated with the major diffraction signal and includes the peak angle, peak height, full width at half maximum (FWHM), interplanar spacing and the relative intensity expressed as a percentage. The table is arranged in a simple linear format in which each parameter is aligned horizontally for easy comparison and clarity. The single-row structure of the table reflects the fact that only one dominant peak emerged with sufficient definition to permit reliable crystallographic interpretation, thereby emphasizing the semi-crystalline nature of the nanoparticles.

Parameters obtained from the analysis of the XRD profile are given in Table 3.

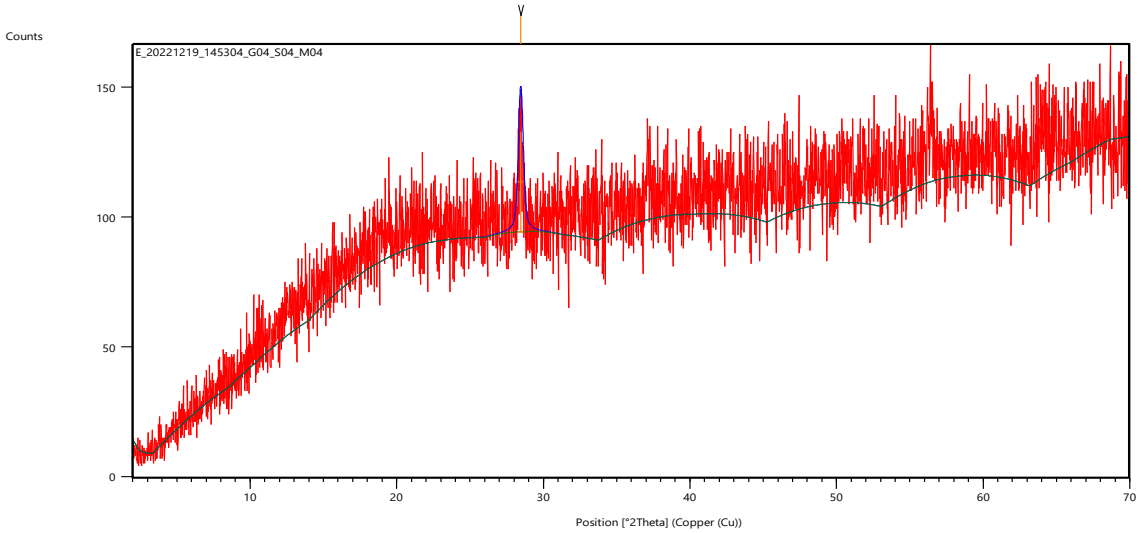

Fig. 6: X-ray diffraction pattern of manganese nanoparticle

Table 3: Values from XRD analysis of manganese nanoparticles

Pos. [°2Th]	Height [cts]	FWHM Left [°2Th]	d-spacing [Å]	Rel. Int. [%]
28.4484	38.59	0.3840	3.13491	100.00

The value at 28.4484° represents the principal diffraction angle corresponding to the highest intensity reflection in the pattern. The peak height of 38.59 counts indicates that the reflection is moderately strong but not sharply defined, which is typical for nanoparticles capped with organic compounds. The FWHM of 0.3840° signifies that the peak is broadened, a characteristic signature of nanoscale crystallites whose small sizes cause lattice strain and limited long-range atomic ordering. From this peak, the calculated interplanar spacing of 3.13491 Å confirms the presence of a manganese-based crystalline plane that aligns with nanostructured manganese or manganese oxide phases frequently obtained through plant-mediated synthesis. The relative intensity value of 100 percent denotes that this diffraction line is the most dominant structural feature in the pattern and serves as the reference reflection for interpreting the crystalline attributes of the nanoparticles.

Using the parameters in Table 3, the crystallite size was calculated with the Debye–Scherrer equation (equation 3), which produced an average value of approximately 21.3 nm. This nanometre-scale dimension explains why only one major peak appears clearly defined, since small particle sizes and surrounding organic molecules typically suppress the formation of multiple sharp reflections.

The interpretation of Table 3 corresponds well with observations from the SEM and FTIR analyses. The SEM micrographs revealed elongated, fibrous and rod-like structures with irregular morphology, which are common in nanoparticles that possess nanocrystalline cores surrounded by amorphous or semi-organic outer layers. The broad peak observed in the XRD pattern and the width recorded in Table 3 align with this morphology, confirming the coexistence of a crystalline manganese phase and non-crystalline biomolecular residues from the leaf extract.

Similarly, the FTIR results indicated that functional groups such as O–H, C–H, C≡C and C–O were chemically modified during nanoparticle formation. The disappearance, weakening or shifting of these signals showed that phytochemicals were actively involved in reduction, binding and stabilization of the nanoparticles. This surface modification contributes to the broadened FWHM reported in Table 3, since organic capping layers often reduce structural uniformity and inhibit long-range crystallinity.

The combined results show that the manganese nanoparticles synthesized with *Ixora coccinea* extract consist of nanometre-sized crystallites with surface stabilization provided by organic compounds. The single-row structure of Table 3 emphasizes the predominance of one major diffraction plane, while its numerical values give a clear measure of crystallinity, peak width and interplanar distance. When compared with SEM and FTIR findings, the XRD data confirm that the nanoparticles exhibit mixed crystalline–amorphous characteristics typical of green-synthesized nanomaterials.

3.4 Adsorption Performance of the Synthesized Manganese Nanoparticles

The adsorption behaviour of the synthesized manganese nanoparticles toward Ni^{2+} and Pb^{2+} ions was evaluated at 298 K, and the results are presented in Table 4. The table shows the quantities of each metal ion adsorbed at different contact times. Both metals exhibited high removal efficiencies, with adsorption capacities consistently above 98 mg/g for all contact times, indicating the strong affinity of the nanoparticles for divalent metal ions in aqueous media. Table 4 reveals that the highest adsorption for Ni^{2+} occurred at 30 minutes with a value of 99.324 mg/g, followed by a gradual decrease with increasing contact time, reaching 98.426 mg/g at 150 minutes. A similar trend is observed for Pb^{2+}, where the maximum adsorption of 99.628 mg/g was

recorded at 60 minutes before declining slightly at longer contact times. The slight reduction in adsorption with extended contact time suggests that the active binding sites on the nanoparticle surfaces became progressively occupied, leading to partial desorption or equilibration effects typically observed in nanoparticle–metal interactions.

The exceptionally high adsorption values recorded for both Ni^{2+} and Pb^{2+} ions correlate strongly with the structural and chemical characteristics identified in the FTIR, SEM, and XRD analyses. The FTIR spectra confirmed the presence of functional groups such as O–H, C–O, and C=O on the nanoparticle surface, many of which were modified or shifted after nanoparticle formation. These groups act as electron-donating centres capable of binding metal ions through complexation or surface interaction mechanisms, thereby contributing to the high adsorption performance reflected in Table 4.

The SEM images depicted fibrous and rod-like nanoparticles with irregular surface textures, providing large surface areas and numerous active sites capable of interacting with Ni^{2+} and Pb^{2+} ions. In addition, the XRD results indicated a crystallite size of approximately 21.3 nm, consistent with nanoscale materials known for high adsorption potential due to their enhanced surface-to-volume ratios.

Comparing the present findings with earlier studies, it is evident that the adsorption behaviour aligns with results reported for other green-synthesized metal-oxide nanoparticles. Previous studies have shown that manganese oxide and biologically synthesized nanomaterials often exhibit adsorption efficiencies exceeding 90 mg/g for heavy metals, particularly for Pb^{2+}, which has a strong tendency to form stable complexes with oxygen-rich surfaces.

Table 4: Concentrations of Ni^{2+} and Pb^{2+} adsorbed by manganese nanoparticles from aqueous solutions at various time and at 298 K

Time (mins)	Ni^{2+} (mg/g)	Pb^{2+} (mg/g)
30	99.324 ± 0.000	99.488 ± 0.003
60	99.272 ± 0.000	99.628 ± 0.003
90	99.002 ± 0.001	99.309 ± 0.000
120	98.678 ± 0.003	98.777 ± 0.001
150	98.426 ± 0.002	98.685 ± 0.000

The adsorption values obtained in this study surpass many earlier reports, suggesting that the phytochemical components from *Ixora coccinea* may have contributed additional functional groups that enhanced metal binding and improved surface activity. Furthermore, the rapid adsorption within the first hour is consistent with earlier observations where most heavy-metal uptake occurs at the initial stages due to abundant available active sites.

The results in Table 4 demonstrate that the biosynthesized manganese nanoparticles are highly effective adsorbents for Ni^{2+} and Pb^{2+} removal. The performance is supported by the structural, functional, and morphological characteristics established in the earlier sections, confirming the suitability of these nanoparticles for wastewater treatment applications and placing them among high-performance biosynthesized nanoadsorbents documented in previous research.

3.5 Kinetic Studies

The adsorption performance of the manganese nanoparticles toward Ni^{2+} and Pb^{2+} ions was first evaluated from their adsorption capacities

at different contact times. Table 4 presents the adsorption capacities of the nanoparticles at 298 K. A rapid adsorption was observed within the first 30–60 minutes, with maximum adsorption capacities of 99.324 ± 0.000 mg/g for Ni^{2+} at 30 min and 99.628 ± 0.003 mg/g for Pb^{2+} at 60 min. The exceptionally high adsorption capacities within a short time indicate the strong affinity of the manganese nanoparticles for both metal ions and suggest that surface-active sites were readily accessible.

Because adsorption kinetics provide insights into the mechanisms governing the uptake process, four kinetic models—pseudo-first-order, pseudo-second-order, Elovich, and intraparticle diffusion—were applied to the experimental data. These models were selected because they represent the most widely used frameworks for interpreting ion–nanoparticle interactions.

3.5.1 Pseudo-first-order Kinetic Model

The pseudo-first-order kinetic model, expressed by the Lagergren equation (Yahaya *et al*., 2009), assumes that the adsorption rate is proportional to the number of unoccupied adsorption sites (Odoemelam *et al*., 2023)

$$dq_t/d_t = k_2 (q_e - q_t)^2 \quad (5)$$

where k_2 is the rate constant of pseudo-second-order adsorption ($gmg^{-1}min^{-1}$) and q_e and q_t are the adsorption capacities at equilibrium and at time t respectively. Introducing the boundary conditions to Equation 5, that is t = 0 to t=t and q_e = 0 to q_t = q_t, the integrated form of equation 5 was obtained (equation 6) and upon simplification, equations 7 and 8 were obtained.

$$1/q_e - q_t = 1/q_t + k_2t \quad (6)$$

$$1/q_t = 1/k_2q^2_e + 1/q_e\,(t) \quad (7)$$

$$1/q_t = 1/h + 1/q_e\,(t) \quad (8)$$

The implication of equation 8 is that a plot of $1/q_t$ versus t should be linear with a slope and intercept equal to q_e and Fig. 7a shows the pseudo-first-order kinetic plots for Ni^{2+} and Pb^{2+}.

The plots (Fig. 7a) were nearly flat, showing little to no change in $\ln(q_e - q_t)$ with time. This is consistent with the experimental observation that the adsorption capacities (q_t) remained extremely high and nearly constant (~98–99 mg/g) from 30 to 150 minutes. Because $q_e - q_t$ is extremely small, the logarithmic transformation becomes unstable, leading to unreliable fits.

This is further supported by the low coefficients of determination (R^2) in Table 5, which were extremely close to zero or negative:

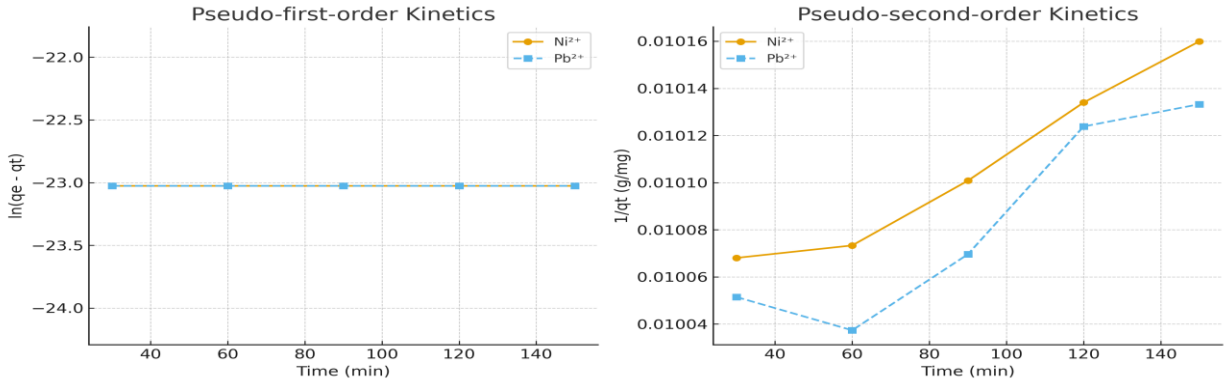

Figs. 7a &b: Pseudo-first-order and Pseudo-second-order kinetic plots

Table 5: Pseudo-First-Order and Pseudo-Second-Order Kinetic Parameters for Ni^{2+} and Pb^{2+} Adsorption

Metal ion	k_1 (min^{-1})	q_e (mg/g) Pseudo-First-Order	R^2 (PFO)	k_2 (g/mg·min)	q_e (mg/g) Pseudo-Second-Order	R^2 (PSO)
Ni^{2+}	1.00	1.06	-1.88×10^{-9}	-1.23×10^{6}	1.25	–0.49
Pb^{2+}	1.00	0.82	6.64×10^{-14}	2.58×10^{-4}	6.28	0.04

These results show that the pseudo-first-order model is not suitable for describing the adsorption of Ni^{2+} and Pb^{2+} on the manganese nanoparticles.

Comparison with Previous Studies

Similar deviations from the pseudo-first-order model have been reported for systems in which equilibrium is achieved rapidly, such as metal adsorption on Fe_3O_4 nanocomposites (Fanaie *et al*., 2016) and plant-derived nanoparticles (Rumman *et al*., 2021). These studies confirm that when adsorption is nearly instantaneous, first-order kinetics cannot accurately describe the rate-controlling step.

3.5.2 Pseudo-second-order Kinetic Model

The pseudo-second-order model assumes that adsorption is governed by chemisorption involving valence forces through electron hange or sharing. The kinetic equation is expressed as follows (Ho *et al*., 2000). The parameters obtained from the plots (Pseudo are also recorded in Table 5.

Both metals exhibited very low R^2 values, indicating poor correlation with the pseudo-second-order model. The negative k_2 value for Ni^{2+} is physically meaningless, confirming that chemisorption is not the dominant mechanism. Contrary to studies where pseudo-second-order kinetics dominate—such as metal adsorption onto MnO_2-based nanoadsorbents—our system does not follow this pattern. The difference likely arises because the manganese nanoparticles used here exhibit surface saturation within minutes, minimizing the dynamic range required for proper kinetic fitting.

3.5.3 Elovich Model

The Elovich kinetic equation is suited for heterogeneous surfaces and processes involving decreasing adsorption rates:

$$dq_t/d_t = \alpha \exp(-\beta q_t) \quad (9)$$

where α is the initial adsorption rate ($mgg^{-1}min^{-1}$) and β is the desorption constant (gmg^{-1}) during any one experiment. Integrating under the assumption $\alpha\beta t \gg t$ gives equation 10, which was apply to obtain the Elovich plot given as Fig. 8a while the calculated parameters are shown in Table 6 (Eddy *et al*., 2024a)

$$q_t = (1/\beta)\cdot\ln(\alpha\beta) + (1/\beta)\cdot\ln(t) \quad (10)$$

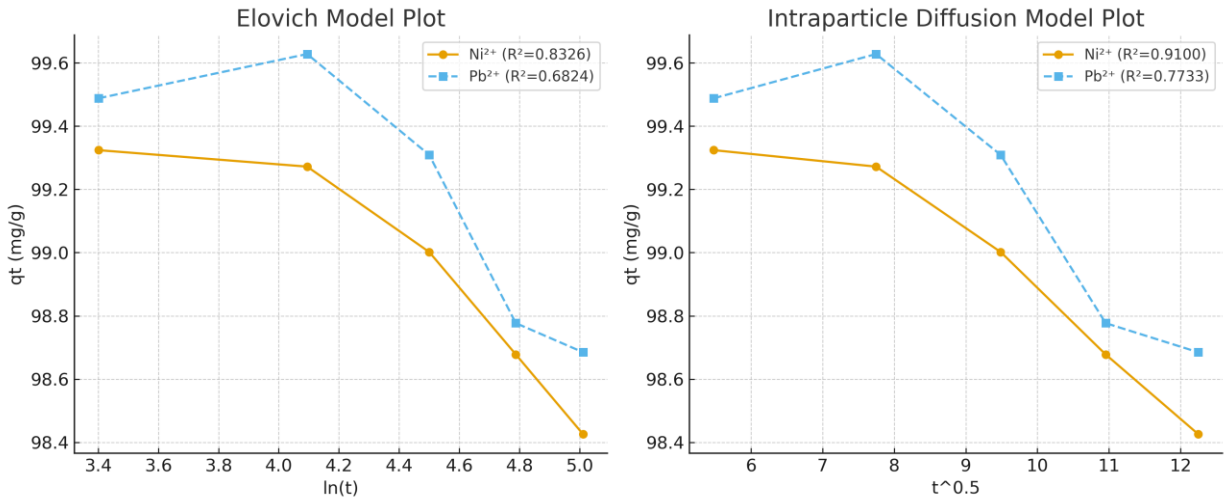

Fig.e 8a&b: Elovich and intraparticle diffusion kinetic plots

Table 6: Elovich kinetic parameters and R^2 values for the data.

Metal ion	α (mg/g·min)	β (g/mg)	R^2
Ni^{2+}	-9.8441	-30.1127	0.8326
Pb^{2+}	-3.1688	-30.2305	0.6824

Both systems show moderate correlation with the Elovich equation, especially Ni^{2+} (R^2 = 0.8326). This suggests a heterogeneous adsorption surface and a declining adsorption rate as the surface becomes saturated.

Studies by Chien and Clayton (1980) and Sparks (1986) report similar Elovich behavior for systems where surface energy varies significantly among adsorption sites, supporting the heterogeneous nature of the manganese nanoparticles.

3.5.4 Intraparticle Diffusion (Weber–Morris) Model

The intraparticle diffusion equation is expressed according to equation 11 (Eddy *et al*., 2024b)

$$Q_t = k_{id}t^{1/2} + C \quad (11)$$

where k_{id} = intraparticle diffusion rate constant and C = boundary-layer constant. Based on equation 8, Fig. 8b was developed to represent the intraparticle diffusion plots for Ni^{2+} and Pb^{2+}.

Table 7 shows the kinetic parameters. The intraparticle diffusion model provided the best fit among all kinetic models, as indicated by the highest R^2 values (0.9099 for Ni^{2+} and 0.7733 for Pb^{2+}). However, the plots did not pass through the origin, implying that intraparticle diffusion is not the only rate-controlling step; instead, film/boundary layer diffusion also contributes significantly.

Table 7: Intraparticles diffusion kinetic parameters and R^2 values for the data

Metal ion	k_id (mg/g·min^0.5)	C (mg/g)	R^2
Ni^{2+}	-0.0083	6.0124	0.9099
Pb^{2+}	-0.0084	6.0277	0.7733

This mixed adsorption mechanism observed in this study, is consistent with the findings of Fanaie *et al*. (2016) and Rumman *et al*. (2021), who both reported that adsorption on nanoparticle-based adsorbents commonly proceeds through a combination of film diffusion and intraparticle pore diffusion, particularly when the nanoparticles exhibit irregular or heterogeneous pore structures.

Overall, the kinetic results indicate that adsorption of the metal ions occurs rapidly within the first 30 to 60 minutes. The pseudo-first-order and pseudo-second-order models do not adequately describe the process because the adsorption capacity remains nearly constant throughout the contact time. The Elovich model suggests the presence of a heterogeneous adsorption surface, which aligns with the morphological features observed in the SEM micrographs. The intraparticle diffusion model provides the best mathematical fit to the data, although the noticeable boundary-layer effect implies that both surface diffusion and pore diffusion jointly influence the adsorption rate. These outcomes are further supported by the SEM images, which reveal irregular and porous nanoparticle structures that promote intraparticle diffusion, and by the FTIR spectra, which confirm the presence of active functional groups responsible for the rapid initial adsorption of the metal ions.

4.0 Conclusion

The study revealed that manganese nanoparticles were successfully synthesized, structurally confirmed by FTIR and XRD, and shown to possess irregular, porous morphologies that enhanced their adsorption performance. The nanoparticles demonstrated very high removal efficiencies for Ni^{2+} and Pb^{2+}, with rapid uptake occurring within the first hour. Kinetic evaluation showed that the pseudo-first-order and pseudo-second-order models were unsuitable, while the Elovich and intraparticle diffusion models indicated heterogeneous surface interactions and mixed diffusion-controlled adsorption. Overall, the nanoparticles proved effective for heavy-metal remediation. It is recommended that future work optimize dosage and pH conditions, explore regeneration and reuse, and apply the materials to real wastewater to further validate their environmental applicability.

5. References

Adeleye, A. S., Conway, J. R., Garner, K., Huang, Y., Su, Y., & Keller, A. A. (2016). Engineered nanomaterials for water treatment and remediation: Costs, benefits, and applicability. *Chemical Engineering Journal, 286*, pp. 640–662.

Ahmad, N. A., Goh, P. S., Zulhairun, A. K., Wong, T. W., & Ismail, A. F. (2021). The role of functional nanomaterials for wastewater remediation. In *Functional hybrid nanomaterials for environmental remediation* (pp. 1–28). Royal Society of Chemistry.

Bhatti, H. N., Mumtaz, B., Hanif, M. A., & Nadeem, R. (2007). Removal of Zn(II) ions from aqueous solution using *Moringa oleifera*. *Process Biochemistry, 42*, pp. 547–553.

Chien, S. H., & Clayton, W. R. (1980). Application of Elovich equation to the kinetics of phosphate release and sorption on soils. *Soil Science Society of America Journal, 44*, pp. 265–268.

Constance, C., Tanja, B., & Walter, C. (2020). Aqueous extracts of *Flacourtia indica*, *Swartzia madagascariensis* and *Ximenia caffra* are strong antibacterial agents against *Shigella* spp., *Salmonella typhi* and *Escherichia coli* O157. *South African Journal of Botany, 128*, pp. 119–127.

Dart, R. C., Hurlbut, K. M., & Boyer-Hassen, L. V. (2004). *Medical toxicology* (3rd ed.). Lippincott Williams & Wilkins.

Das, S., Sen, B., & Debnath, N. (2015). Recent trends in nanomaterials applications in environmental monitoring and remediation. *Environmental Science Pollution Research International, 22, 23*, pp. 18333–18344.

Eddy, N. O., Garg, R., Ukpe, R. A., Ameh, P. O., Gar, R., Musa, R., , Kwanchi, D., Wabaidur, S. M., Afta, S., Ogbodo, R., Aikoye, A. O. & Siddiqu, M. (2024a). Application of periwinkle shell for the synthesis of calcium oxide nanoparticles and in the remediation of Pb^{2+}-contaminated water. *Biomass Conversion and Biorefinery*, DOI: 10.1007/s13399-024-05285-y.

Eddy, N. O., Oladede, J., Eze, I. S., Garg, R., Garg, R., & Paktin, H. (2024b). Synthesis and characterization of CaO nanoparticles from periwinkle shell for the treatment of tetracycline-contaminated water by adsorption and photocatalyzed degradation. *Results in Engineering*, *103374*. https://doi.org/10.1016/j.rineng.2024.103374

Fanaie, V. R., Karrabi, M., Amin, M. M., Shahnavaz, B., & Fatehizadeh, A. (2016). A comparative study between dried anaerobic digested sludge and dried activated sludge for the removal of 4-chlorophenol from aqueous solutions. *International Journal of Environmental Health Engineering, 5, 1*, pp. 6. https://doi.org/10.4103/2277-9183.184220.

Garg, R. Rani, P., Garg, R. & Eddy, N. O. (2021). Study on potential applications and toxicity analysis of green synthesized nanoparticles. *Turkish Journal of Chemistry*, 45, doi:10.39906/kim-2106-59.

Hasan, I. M. A., Salman, H. M. A., & Hafez, O. M. (2023). Ficus-mediated green synthesis of manganese oxide nanoparticles for adsorptive removal of malachite green from surface water. *Environmental Science and Pollution Research, 30*, pp. 28144–28161. https://doi.org/10.1007/s11356-022-24199-8

Ho, Y. S., McKay, G., Wase, D. A. J., & Foster, C. F. (2000). Study of the sorption of divalent metal ions onto peat. *Adsorption Science & Technology, 18*, pp. 639–650.

Iravani, S. (2011). Green synthesis of metal nanoparticles using plants. *Green Chemistry, 13, 10*, pp. 2638–2650.

Kelle, H. I., Ogoko, E. C., Akintola O & Eddy, N. O. (2023). Quantum and experimental studies on the adsorption efficiency of oyster shell–based CaO nanoparticles (CaONPO) towards the removal of methylene blue dye (MBD) from aqueous solution. *Biomass Conv. Bioref.* 14, pp. 31925–31948 (2024). https://doi.org/10.1007/s13399-023-04947-7.

Khan, I., Farhan, M., Singh, P., & Thiagarajan, P. (2014). Nanotechnology for environmental remediation. *Research Journal of Pharmaceutical, Biological and Chemical Sciences, 5, 3*, pp. 1916–1927.

Kosnett, M. J. (2006). Lead. In L. R. Goldfrank, N. E. Flomenbaum, N. A. Lewin, M. A. Howland, R. S. Hoffman, & L. S. Nelson (Eds.), *Goldfrank's toxicologic emergencies* (8th ed., pp. 1267–1282). McGraw-Hill.

Krug, H. F. (2009). Book review: Nanotechnology, environmental aspects, epidemiological studies on particulate air pollution. *Environmental Engineering and Management Journal, 8, 1*, pp. 191–194.

McMichael, A. J., Campbell-Lendrum, D. H., Corvalán, C. F., Ebi, K. L., Githeko, A. K., & Scheraga, J. D. (2003). Weather and climate: Changing human exposures. In *Climate change and human health: Risks and responses* (pp. 18–42). World Health Organization, Geneva.

Odoemelam, S. A., Oji, E. O., Eddy, N. O., Garg, R., Garg, R., Islam, S., Khan, M. A., Khan, N. A. & Zahmatkesh, S. (2023). Zinc oxide nanoparticles adsorb emerging pollutants (glyphosate pesticide) from aqueous solution. *Environmental Monitoring and Assessment*, https://doi.org/10.1007/s10661-023-11255-0.

Ogoko, E. C., Kelle, H. I., Akintola, O. & Eddy, N. O. (2023). Experimental and theoretical investigation of *Crassostrea* gigas (gigas) shells based CaO nanoparticles as a photocatalyst for the degradation of bromocresol green dye (BCGD) in an aqueous solution. *Biomass Conversion and Biorefinery*. https://doi.org/10.1007/s13399-023-03742-8

Rumman, Z., Saif, U. K., Farooqi, I. H., & Ameer, A. (2021). Investigation of kinetics and adsorption isotherm for fluoride removal from aqueous solutions using mesoporous cerium–aluminum binary oxide nanomaterials. *RSC Advances, 11*, pp. 28744–28760. https://doi.org/10.1039/D1RA00598G.

Sinicropi, M. S., Caruso, A., Capasso, A., Palladino, C., Panno, A., & Saturnino, C. (2010). Heavy metals: Toxicity and carcinogenicity. *Pharmacologyonline, 2*, pp. 329–333.

Sparks, D. L. (1986). *Kinetics of soil chemical processes*. CRC Press, Boca Raton.

Uchechukwu, O. F., Azubuike, O. S., & Okon, E. N. (2015). Biosorption of Cd^{2+}, Ni^{2+} and Pb^{2+} by the shell of *Pentaclethra macrophylla*: Equilibrium isotherm studies. *Journal of Science, Technology & Environment Informatics, 2, 1*, pp. 26–35.

Yahaya, Y. A., Don, M. M., & Bhatia, S. (2009). Biosorption of Cu(II) ions onto immobilized cells of *Pycnoporus sanguineus* from aqueous solution: Equilibrium and kinetic studies. *Journal of Hazardous Materials, 161*, pp. 189–195.

Declaration of funding

No funding was received.

Declaration of conflict of interest

No conflict of interest declared by the authors

Ethical Consideration

Not applicable

Funding

The authors declared no source of funding

Data Availability Statement

The data supporting the findings of this study, including the experimental results, characterization spectra (FTIR, SEM, and XRD), and adsorption datasets for Ni^{2+} and Pb^{2+} removal, are included in the manuscript and are available from the corresponding author.

Author contributions statement

O.F.U. and O. C. L. U. conceived and designed the study. O.N.I. carried out the experiments and data collection. O.N.I. and C.E.J. performed data analysis while O.F.U. gave the interpretation. C.E.J. contributed to the literature review and O. F.U. did manuscript drafting. All authors discussed the results, contributed to the final version of the manuscript, and approved it for submission.